Fast Frequency Regulation Method of PV System Based on Feedforward of VPPT Reference Value

Wenqiang Xie[1], Ziran Guo[1], Xiaolong Xiao[1], Xiaoxing Lu[1], Fangfang Zhu[1]
[1]State Grid Jiangsu Electric Power Co. Ltd. Research Institute, Nanjing, China
Corresponding author: Wenqiang Xie (e-mail: bjxiewenqiang@163.com).

ABSTRACT High penetration of photovoltaic (PV) generation reduces the frequency regulation margin of power systems because inverter-based resources contribute little inherent inertia. Conventional active power reserve (APR) schemes can provide droop-based primary frequency support, but the typical 0.6–3s power-tracking delay makes them unable to deliver timely inertial power to arrest fast frequency ramps. Since PV converters can change power on the millisecond (ms) scale, the dominant limitation is the power-tracking algorithm. This paper proposes a fast frequency regulation method based on feedforward updates of the power-tracking reference: the variable power point tracking (VPPT) algorithm handles slow frequency deviations, while a feedforward branch responds to rapid fluctuations to provide inertia support. A frequency response model is developed to examine impacts on both common-mode and differential-mode frequency components. Compared with conventional VPPT-based regulation, simulations show that the proposed controller reduces peak RoCoF and maximum frequency deviation and attenuates frequency differential-mode components.

INDEX TERMS Variable power point tracking, Feedforward control, Primary frequency regulation, Photovoltaic power generation, Virtual inertia, Frequency response.

I. INTRODUCTION

UNDER China's county-scale photovoltaic development policy, solar generation is expected to become a major form of future energy supply. It is projected that by 2030 the combined installed capacity of wind and solar power will exceed 1.2 billion kilowatts [1]. However, as high shares of PV replace synchronous generation, overall inertia and primary frequency response decline, which can compromise frequency stability [2]. Historical events such as the UK blackout on 9 August 2019 and the South Australia disturbance on 28 September 2016 illustrate that insufficient primary response and inertia can trigger under-frequency load shedding and wide-area outages [3]. Accordingly, many regions with high renewable penetration now require renewable generator units to provide frequency support [4], [5]. In China, the technical specification for grid-source coordination (DL/T1870-2018) defines requirements for "primary frequency regulation technology for renewable energy," which can be achieved by maintaining active power headroom or by deploying energy storage together with suitable control systems.

Energy storage is commonly used to smooth PV output fluctuations and to exchange active power rapidly during grid frequency disturbances [6], [7]. Many studies have investigated sizing and control of storage devices for renewable units [8]–[10], and demonstration projects have been implemented in China [11]. Nevertheless, practical deployments still leave room for improvement in capacity allocation and overall economic performance.

The APR approach keeps the PV plant intentionally derated so that it retains upward regulating headroom for frequency control. APR avoids the high investment and maintenance costs associated with batteries and is also attractive in regions where PV curtailment ("abandoned light") occurs. Its main drawback is reduced energy yield. References [12]–[14] investigate VPPT-based standby operation and flexible power-point tracking, and [15], [16] study droop-based primary frequency regulation enabled by APR. Field demonstrations of APR frequency regulation are reported in [17]. However, because tracking algorithms must trade off speed and accuracy when selecting perturbation step size and period, typical engineering settings use voltage steps of 1–10 V and perturbation periods of 0.5–2s [17], [18]. As a result, APR PV units respond more slowly than storage-based schemes and cannot provide fast inertial support during rapid frequency events.

Overall, prior work has validated two main solutions for renewable frequency support: energy storage and APR-based headroom control. For large-scale renewable participation, coordinating these solutions (or combining them with other measures) to achieve an overall optimum in technical performance and cost remains a pressing practical problem [11]. For example, [19] shows that coordinating battery storage with APR can be economical for mitigating PV power fluctuations, and [20] proposes coordinated control of variable power tracking and supercapacitor energy storage to enable wind turbines to participate in primary frequency regulation. From the control perspective, however, energy storage can change power almost instantaneously, whereas existing APR schemes are constrained by tracking dynamics. This mismatch in response speed can limit the benefit of coordinated schemes, especially for inertia support.

To address the response-speed bottleneck of APR control, this paper develops a fast primary frequency regulation and inertia-support strategy for PV units based on feedforward updates of the power-tracking command. The controller selects its operating mode according to RoCoF: during slow frequency variations, VPPT is used to provide accurate regulating power; during fast frequency ramps, the feedforward branch generates rapid power commands for inertia support. Frequency-response modeling and simulation results demonstrate that the proposed method shortens the regulation power response of APR PV units and can achieve a response speed comparable to that of energy storage devices. The method improves system frequency dynamics and suppresses frequency differential-mode components, providing useful guidance for upgrading large-scale PV plants for active support.

II. DYNAMIC RESPONSE CHARACTERISTICS OF PV UNITS

The structure of a grid-connected photovoltaic power generation system operating under APR control is shown in Fig. 1. The APR control strategy is formulated based on the intrinsic output characteristics of photovoltaic units. From the perspective of P-U characteristics, stable operation of a photovoltaic unit is maintained on the higher-voltage side of the curve, whereas operation on the lower-voltage side may introduce instability, as reported in previous studies [16].

As illustrated by the P-U characteristic curve in Fig. 2, point M represents the maximum power point of the photovoltaic unit during normal operation, with an output power of P_M. To enable participation in frequency regulation, the PV unit is deliberately operated away from point M. Point A denotes the APR operating point obtained after applying a power curtailment ratio of $d\%$, and the corresponding output power is P_A. During periods of system frequency increase, the operating point may further shift toward point B, which corresponds to the minimum active power level available for frequency regulation support.

According to the national standard "General Principles for Virtual Synchronous Machine Technology" [21], renewable energy units participating in frequency regulation should be capable of adjusting their active power output by no less than 10% of the rated power P_N. In this work, the power

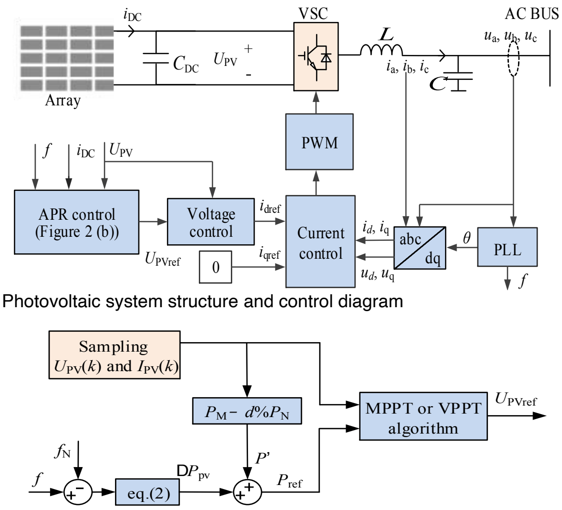

(a) Photovoltaic system structure and control diagram

(b) APR control block diagram

FIGURE 1. Structure and control block diagram of PV generation system in APR mode

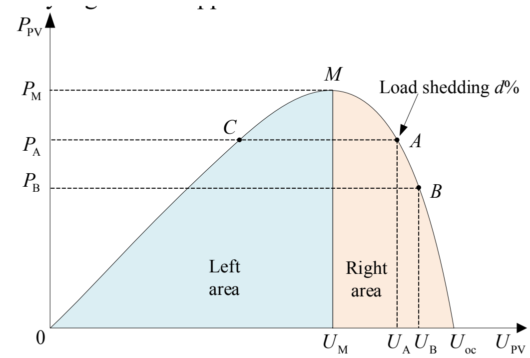

FIGURE 2. P-U characteristics of PV generation system

curtailment ratio is therefore set to $d = 10\%$ to ensure adequate regulation margin for both upward and downward frequency support.

To enable photovoltaic units to participate in primary frequency regulation, a frequency control loop with droop characteristics is introduced, as shown in Fig. 1(b) [3]. At the initial stage of operation, the maximum power point tracking (MPPT) algorithm is employed to extract the maximum available power from the photovoltaic array. Subsequently, the control mode is switched to VPPT, allowing the operating point to move from point M to the reserved operating point A after power curtailment.

Under APR operation, the reference power of the photovoltaic unit is expressed by (1), where P_{ref} denotes the active power reference value. The operating condition of the photovoltaic unit is determined according to the grid-side frequency deviation, defined as $\Delta f = f - f_N$. When no frequency disturbance is detected, the photovoltaic unit maintains operation at the APR point A. Once the frequency deviation exceeds the dead-band threshold of ± 0.033 Hz

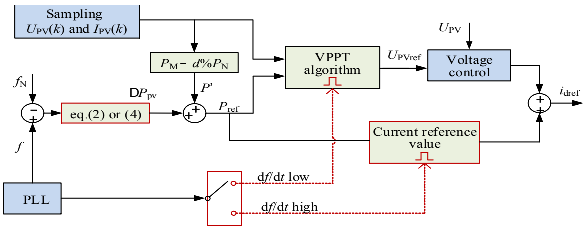

FIGURE 3. Block diagram of feedforward control for power command tracking

[22], the primary frequency regulation loop is activated, and the corresponding power adjustment ΔP_{PV} is calculated according to (2).

$$P_{\mathrm{ref}} = P_M - d\%P_N + \Delta P_{\mathrm{PV}} \tag{1}$$

$$\Delta P_{\mathrm{PV}} = \begin{cases} 0, & |\Delta f| < 0.033\,\mathrm{Hz}, \\ -k_f \Delta f, & 0.033\,\mathrm{Hz} \le |\Delta f| \le \dfrac{d\%P_N}{k_f}, \\ -d\%P_N, & \Delta f > \dfrac{d\%P_N}{k_f}, \\ d\%P_N, & \Delta f < -\dfrac{d\%P_N}{k_f}. \end{cases} \tag{2}$$

In (2), k_f represents the primary frequency regulation coefficient, f is the measured grid frequency, and f_N is the rated system frequency. Through this mechanism, the photovoltaic unit provides proportional active power support in response to system frequency deviations. Nevertheless, the dynamic performance of this frequency regulation process remains constrained by the response speed of the VPPT algorithm, which motivates the development of faster control strategies presented in the subsequent sections.

III. FEEDFORWARD CONTROL FOR POWER COMMAND TRACKING

A fast frequency regulation strategy for PV units based on feedforward control of the power command is illustrated in Fig. 3. In this strategy, the conventional VPPT algorithm is retained to respond to slow frequency variations, while an additional feedforward control path is introduced to cope with rapid frequency fluctuations. By coordinating these two mechanisms, both primary frequency regulation and inertia support functions can be achieved.

The disturbance type is identified according to the characteristics of grid-side frequency variations. When the absolute frequency deviation satisfies $|\Delta f| \le 0.033$ Hz, the system is considered to operate under normal conditions, and the photovoltaic unit remains at the APR operating point A. When $|\Delta f|$ exceeds 0.033 Hz, different control modes are activated depending on the rate of change of frequency. In this context, virtual inertia support is realized by utilizing frequency-derivative-related signals, and the corresponding inertia power reference ΔP_H is defined as shown in (3)

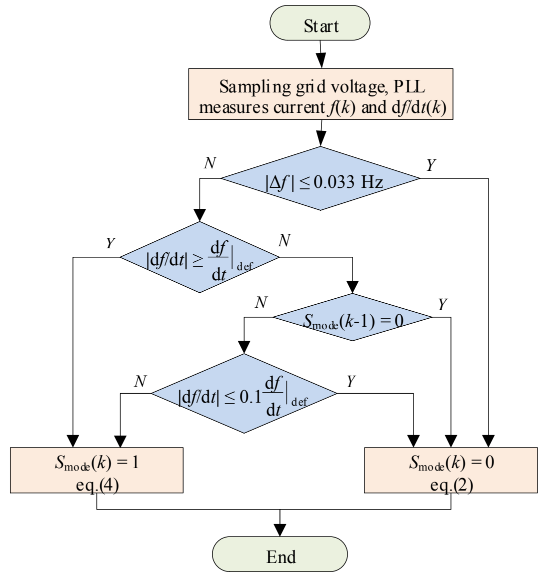

FIGURE 4. Flow chart of feedforward control for power command tracking

[24], where k_H denotes the virtual inertia coefficient and τ_f represents the filter time constant.

$$\Delta P_H = \frac{-k_H\, df/dt}{\tau_f s + 1} \tag{3}$$

During frequency disturbances, the rate of change of grid frequency df/dt can be obtained in real time using a phase-locked loop (PLL)–based measurement method [24]. When the measured df/dt exceeds a predefined threshold, the power command feedforward loop is enabled, and the conventional APR control based on VPPT is temporarily disabled. In this case, the mode signal is set to $S_{\mathrm{mode}} = 0$, and the active power adjustment ΔP_{PV} is calculated according to (4). By directly modifying the power command, the photovoltaic unit can respond rapidly to frequency transients without being limited by the perturbation cycle of the VPPT algorithm.

When the rate of change of frequency decreases below the preset threshold, the feedforward control loop is deactivated. The control strategy then switches back to the VPPT-based APR mode, with the mode signal updated to $S_{\mathrm{mode}} = 1$, and the power adjustment ΔP_{PV} recalculated using (2). Through this switching mechanism, fast response during severe disturbances and accurate power regulation under mild frequency variations are both ensured.

In summary, the overall flow of the feedforward control strategy for power command tracking is depicted in Fig. 4. The proposed control framework enables photovoltaic units to provide rapid inertia-like frequency support while maintaining stable operation and precise power regulation during steady-state and slow dynamic conditions.

IV. FREQUENCY RESPONSE MODELING AND ANALYSIS

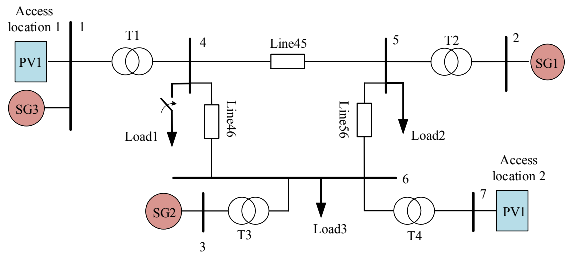

FIGURE 5. Test system

A. FREQUENCY RESPONSE MODEL

In multi-units power systems, small-signal frequency dynamics can be separated into one common-mode (system-average) frequency component and several differential-mode components. The common-mode frequency represents the overall system frequency trajectory governed by the aggregated dynamics of synchronous machines and converter-based resources. Differential-mode frequencies describe relative-frequency interactions among units, which may be excited by parameter mismatches or heterogeneous control structures; suppressing these modes is important for enhancing stability.

The test system is illustrated in Fig. 5, comprising three synchronous generators (SGs) and one PV unit. This section conducts theoretical analysis under the scenario where the PV unit is connected to Bus 1 and SG3 is out of service.

Following the modeling approach in [27], a frequency response model is established for the test system. Under a single-machine grid-connected representation, the block diagrams in Fig. 6(a) and Fig. 6(b) describe the active-power responses of the PV unit and the synchronous generator (SG) to angular-frequency disturbances, with the corresponding transfer functions given in (5)–(7).

$$Y_{\mathrm{PV1}} = \frac{-K_{S\_\mathrm{pv}}\omega_N(k_H s + k_f)e^{-\tau_0 s}}{k_H s^2 e^{-\tau_0 s} + k_f s e^{-\tau_0 s} + 2\pi K_{S\_\mathrm{pv}}\omega_N(\tau_f s + 1)} \tag{5}$$

$$\begin{aligned} Y_{\mathrm{SG1}} = &-\frac{\omega_N}{K_{J1}s^2 + (K_{D1} - G_{\mathrm{GOV1}})s + K_{S1}} \\ &\times \big(K_{J1}K_{D1}s^2 + K_{J1}K_{S1}s \\ &\qquad - G_{\mathrm{GOV1}}K_{D1}s - G_{\mathrm{GOV1}}K_{S1}\big) \end{aligned} \tag{6}$$

$$\begin{aligned} Y_{\mathrm{SG2}} = &-\frac{\omega_N}{K_{J2}s^2 + (K_{D2} - G_{\mathrm{GOV2}})s + K_{S2}} \\ &\times \big(K_{J2}K_{D2}s^2 + K_{J2}K_{S2}s \\ &\qquad - G_{\mathrm{GOV2}}K_{D2}s - G_{\mathrm{GOV2}}K_{S2}\big) \end{aligned} \tag{7}$$

Here, K_J denotes the SG inertia coefficient, K_D represents the SG damping coefficient, K_S is the SG synchronous torque coefficient, K_{S_PV} is the PV unit synchronous torque coefficient, and ω_c is the angular frequency of the infinite bus [27]. The parameter τ_0 is the time constant of the delay link $e^{-\tau_0 s}$, which characterizes the time delay induced by the power tracking step size. For VPPT-based primary frequency regulation, τ_0 corresponds to the disturbance time step; for the fast frequency regulation method using feedforward control, τ_0 is approximately zero. $G_{\mathrm{GOV}}(s)$ denotes the governor transfer function, whose model is presented in Fig. 6(c) [28].

For the example system, the transfer functions of the angular-frequency responses of SG1 and SG2 to a load active-power disturbance are expressed in (8) and (9).

$$B_{\omega,1}(s) = \frac{-(K_{J1}s - G_{\mathrm{GOV1}})Y_{\mathrm{SG1}}(s)\omega_N}{Y_{\mathrm{SG1}}(s) + Y_{\mathrm{SG2}}(s) + Y_{\mathrm{PV1}}(s)} \tag{8}$$

$$B_{\omega,2}(s) = \frac{-(K_{J2}s - G_{\mathrm{GOV2}})Y_{\mathrm{SG2}}(s)\omega_N}{Y_{\mathrm{SG1}}(s) + Y_{\mathrm{SG2}}(s) + Y_{\mathrm{PV1}}(s)} \tag{9}$$

Based on Equations (8) and (9), the performance metrics of the fast frequency regulation control schemes can be analyzed and compared across three proposed schemes:
Scheme 1: Droop-based primary regulation with conventional power-command tracking (Fig. 1(b));
Scheme 2: Feedforward-enhanced tracking providing both inertia support and primary regulation (Fig. 4);
Scheme 3: PV units do not participate in frequency regulation.

B. COMMON-MODE COMPONENT OF FREQUENCY

Common-mode frequency response refers to the average value of the frequency response of the generator sets in the power system, also known as the center frequency of inertia. The common-mode frequency response is assessed with the three standard indices: the peak RoCoF, the maximum frequency deviation, and the steady-state frequency offset [20], [29]. Smaller values of these indices indicate better frequency regulation. These indices are therefore used to quantify how the proposed fast frequency regulation strategy improves the common-mode response. With matched inertia parameters, SG1 and SG2 exhibit identical angular-frequency responses.

C. DIFFERENTIAL-MODE COMPONENT OF FREQUENCY

By setting mismatched inertia parameters for SGs, Fig. 7 presents the Bode plot of the angular frequency response. A differential-mode frequency component emerges in Fig. 7, with its peak frequencies at 14 rad/s. Scheme 1 has no impact on the resonant peak of the differential-mode component, whereas Scheme 2 effectively mitigates it. Therefore, Scheme 2 can suppress fluctuations in both the common-mode and differential-mode frequency components simultaneously.

Tab. I compares the technical performance of two frequency regulation schemes. It can be concluded that although the variable power tracking control method provides regulating power, its response time lag prevents effective suppression of frequency rate of change, maximum frequency deviation, and differential-mode components. In contrast, the fast frequency regulation method based on power instruction feedforward demonstrates superior frequency regulation effects across the entire frequency band, offering technologically more comprehensive performance.

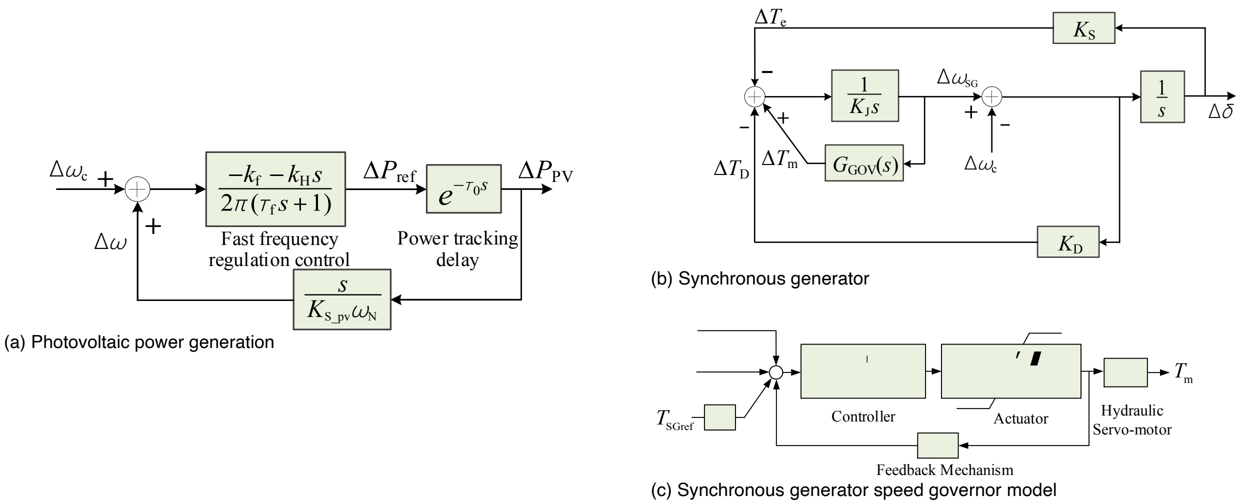

FIGURE 6. Frequency response model

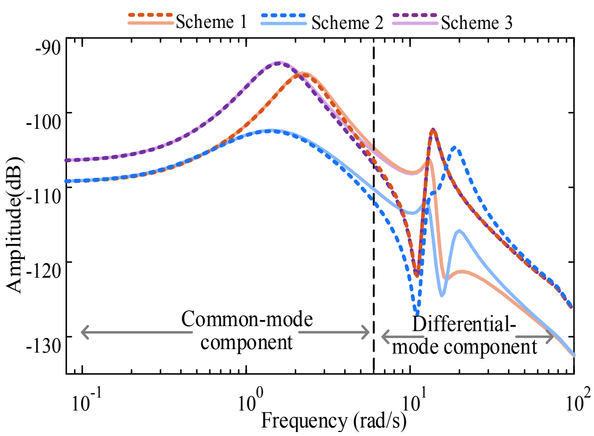

FIGURE 7. Bode diagrams of angular frequency response with mismatched inertia parameters

TABLE I. Technical comparison of the two application modes

Technical indicators	Scheme 1	Scheme 2
Control structure	simple	relatively complex
Response speed	slow	fast
Maximum frequency deviation suppression effect	relatively ineffective	effective
Frequency steady-state deviation suppression effect	effective	effective
RoCoF suppression effect	ineffective	relatively effective
Frequency differential-mode component suppression effect	ineffective	relatively effective

V. SIMULATION ANALYSIS

A. SIMULATION PARAMETERS

In the simulations, the frequency modulation depth is set to $\Delta f_{\max} = \pm 0.2$ Hz, and the PV frequency regulation capacity is limited to 10% of rated power. The total regulation power is defined as the sum of virtual inertia power and primary frequency regulation power; therefore, the droop coefficient and inertia coefficient are calculated from (10). Simulation parameters are listed in Appendix Tab. A. The initial irradiance is 850 W/m^2 and temperature is 25 °C. The VPPT algorithm parameters are configured as follows: perturbation time step = 0.5 s, perturbation magnitude step size ranges from 1 V to 5 V. Parameters for the synchronous generator, governor, and excitation controller are referenced from literature. Simulation scenarios are shown in Tab. II. When analyzing the impact of load disturbance magnitude and PV unit inertia coefficient in Sections 4.2 and 4.3, the operating conditions are set as: PV connected to bus 1 of the test system with SG3 out of service. For analyzing the impact of different connection locations in Section 4.3, the operating conditions are set as: PV connected to bus 1 or bus 7 with SG3 in service.

The RoCoF limit is determined based on the system's inertia level and load disturbance magnitude ΔP_{load}. For the test system, the total inertia is J_Σ, and the defined load disturbance power threshold is $\Delta P_{\text{load\_ref}}$. Through approximate calculation, the maximum RoCoF value is derived. In this study, the SG's total inertia is $J_\Sigma = 84.4\,\text{kg}\cdot\text{m}^2$, and the defined load disturbance threshold is 150 kW. Thus, the coefficient $df/dt|_{\text{def}} = 0.75$ Hz/s is calculated, and the RoCoF limit is set to 0.8 Hz/s. When the disturbance exceeds the defined load disturbance threshold, the RoCoF reaches this limit, and power tracking feedforward control is activated to achieve fast frequency regulation.

$$\begin{cases} k_f = \dfrac{10\% P_N}{\Delta f_{\max}}, \\ k_H = \dfrac{10\% P_N}{\max(df/dt)}. \end{cases} \tag{10}$$

TABLE II. Simulation cases

Simulation cases	0 s	10.2 s	17.2 s
Frequency regulation under load changes	Enable APR algorithm	Sudden load increase/decrease of 270 kW or 150 kW	–
Frequency regulation under changes in lighting conditions	Enable APR algorithm	Irradiance increases by 250 W/m^2	Irradiance decreases by 600 W/m^2

B. ADJUSTMENT OF FREQUENCY COMMON MODE COMPONENT UNDER IRRADIANCE VARIATION

The stability of the proposed fast frequency regulation control scheme is verified under varying irradiance conditions. When irradiance changes, PV units may operate in the left half-plane (unstable region), degrading system frequency response. To address this, the minimum operating voltage is set to 20V below the maximum power point voltage (U_M), i.e., $U_{\text{limit}} = U_M - 20\text{V}$. When the real-time measured DC voltage drops below U_{limit}, the PV system immediately switches its control mode from variable power tracking or fast frequency regulation back to MPPT mode [15]. The operating conditions for sudden irradiance variation scenarios are configured as shown in Tab. II. Simulation results for Scheme 1 and Scheme 2 are presented in Fig. 8. The PV characteristic curves and actual operational trajectories of the PV system are illustrated in Fig. 9, where (a) corresponds to Scheme 1 and (b) to Scheme 2.

C. SUPPRESSION OF FREQUENCY DIFFERENCE-MODE COMPONENTS UNDER LOAD CHANGES

When multiple SGs exhibit mismatched inertia parameters, the system frequency response will contain differential-mode components. To verify the effectiveness of the fast frequency regulation method in suppressing frequency differential-mode components, mismatched SG inertia parameters are intentionally configured. For intuitive and quantitative analysis, the common-mode component is characterized by the average frequency of multiple SGs, while the differential-mode component is represented by the frequency deviations among SGs.

Fig. 10 shows the frequency response waveforms under a sudden load increase. The corresponding common-mode and differential-mode frequency response performance metrics are presented in Tab. III. For the common-mode component, two indicators are calculated: maximum frequency deviation and peak RoCoF. For the differential-mode component, the maximum amplitude of frequency relative deviation is computed. It can be observed that both schemes exhibit frequency differential-mode components during load disturbances. After 2 seconds of attenuation, the differential-mode component 1 (with a fluctuation period about 0.61 s) no longer exists in the frequency responses of either scheme. However, Scheme 1 still contains another differential-mode component (differential-mode component 2, with a fluctuation period about 0.5 s), which is consistent with the

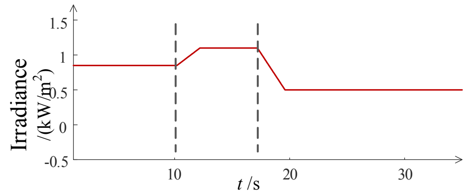

Irradiance curve

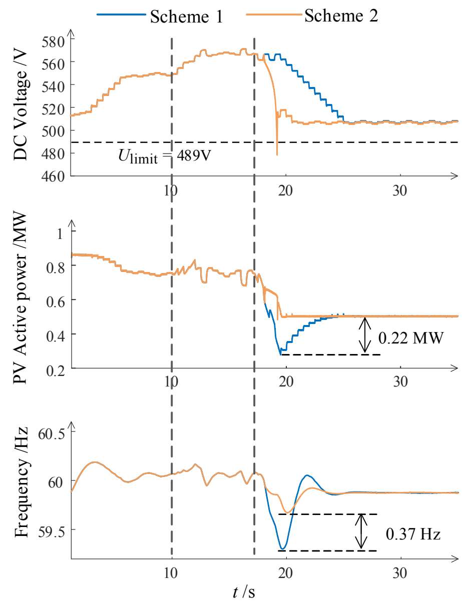

Response waveform of PV units

FIGURE 8. Frequency regulation under irradiance fluctuation

perturbation time step of the VPPT algorithm and caused by large-step tracking. Therefore, Scheme 2 (the fast frequency regulation control scheme) effectively eliminates differential-mode component 2. After increasing the inertia response, it reduces both the common-mode frequency change rate and the maximum amplitude of the differential-mode frequency, demonstrating a certain inhibitory effect on differential-mode component 1. Additionally, comparing Fig. 12(a) and (b), when the load disturbance increases, the transient frequency deviation in Fig. 12(b) exceeds 0.2 Hz. During this period, although the PV units cannot further increase their frequency regulation output and operate near the maximum power point M, they still exhibit certain common-mode and differential-mode frequency regulation effects.

For a 150 kW sudden load increase, Fig. 11 compares PV frequency responses obtained with different virtual inertia coefficients, and Tab. IV summarizes the corresponding common-mode and differential-mode indices. The inertia coefficient has a significant impact on dynamic performance: increasing it reduces the maximum frequency deviation and RoCoF, and also lowers the relative frequency oscillation amplitude between units. However, because PV headroom is limited to 10% of rated power, the incremental benefit diminishes as the inertia coefficient continues to increase.

TABLE III. Comparison of common-mode and different-mode frequency response performance under load sudden increase

Indicators	Sudden load increase of 150 kW			Sudden load increase of 270 kW		
	Scheme 1	Scheme 2	Scheme 3	Scheme 1	Scheme 2	Scheme 3
Maximum of $(f_2 - f_1)$ /Hz	0.038	0.022	0.040	0.072	0.047	0.073
Maximum of $0.5(f_2 - f_1)$ /Hz	0.263	0.192	0.322	0.519	0.372	0.578
Maximum of RoCoF /Hz/s	0.693	0.428	0.758	1.352	0.889	1.353

TABLE IV. Frequency response performance under different inertia coefficients

Indicators	Scheme 1	Scheme 2	Scheme 3
Maximum of $(f_2 - f_1)$ /Hz	0.023	0.192	0.041
Maximum of $0.5(f_2 - f_1)$ /Hz	0.243	0.233	0.322
Maximum of RoCoF /Hz/s	0.428	0.365	0.758

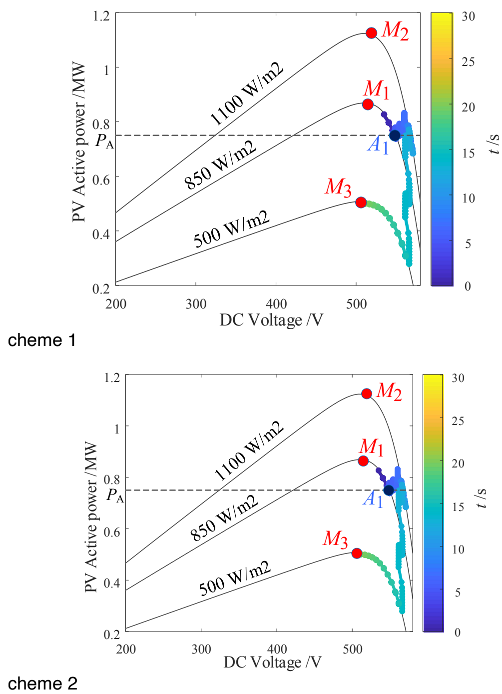

FIGURE 9. P-U characteristic curves and operation trajectory diagrams of PV units

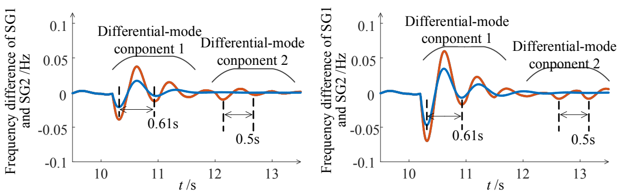

FIGURE 10. Different-mode frequency response under load step disturbance (increase)

When a sudden load increase of 270 kW occurs, the differential-mode frequency responses of PV units under bus 1 and bus 7 integration scenarios are illustrated in

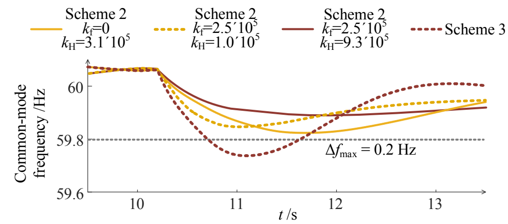

FIGURE 11. Frequency response with different inertia coefficients of PV Units

Fig. 12, with corresponding frequency response performance indicators shown in Tab. V. The results indicate that the maximum frequency deviation consistently occurs between SG1 and SG2 across all control schemes. Scheme 1 exhibits negligible suppression of differential-mode components, while Scheme 2 effectively reduces the amplitude of differential-mode components. Under different bus integration conditions, Scheme 3 demonstrates varying degrees of differential-mode suppression. Notably, with PV units integrated at bus 7, frequency deviations between SG1–SG3 are significantly mitigated. In contrast, when PV units are connected to bus 1, Scheme 2 achieves exceptional suppression of differential-mode components between SG1 and SG3 (with near-zero maximum frequency deviation), but inadvertently increases the frequency difference between SG2 and SG3, where the maximum deviation exceeds that observed in Scheme 1. This highlights that the integration location of PV units critically influences the differential-mode suppression performance of Scheme 2.

VI. CONCLUSION

This study develops a feedforward-enhanced fast frequency regulation strategy for APR-operated PV units. By comparing a conventional VPPT-based frequency regulation scheme with the proposed control, the following conclusions are obtained. In terms of frequency regulation functionality, feedforward control can significantly reduce the frequency regulation power response and rise time of PV units, thereby enhancing their rapid power support capability. In terms of frequency regulation effects, the proposed fast

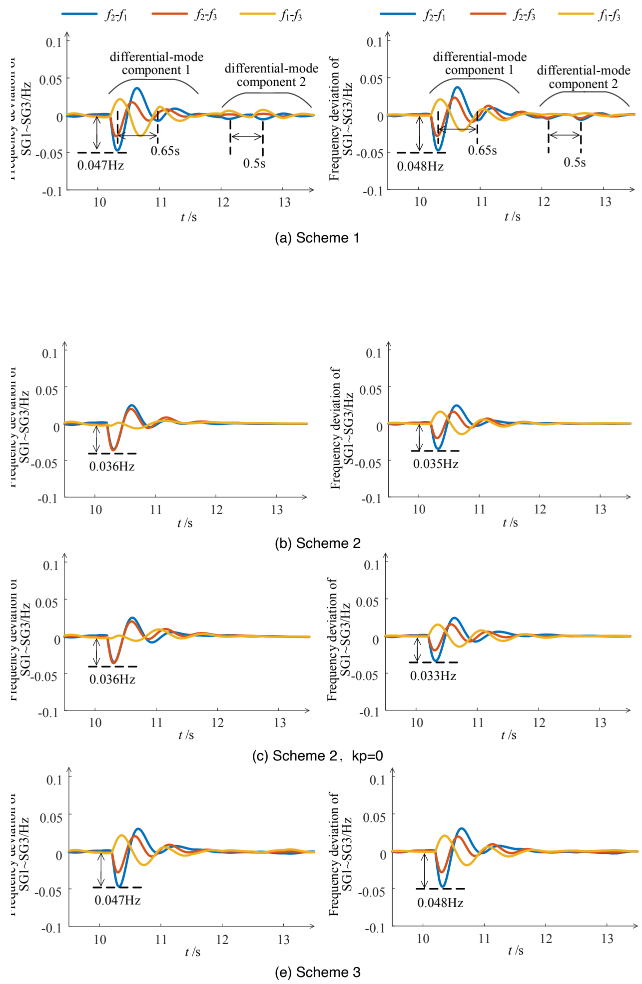

FIGURE 12. Different-mode frequency response under different connection nodes of PV System (Left column: PV is integrated to Bus 1, Right column: PV is integrated to Bus 7)

TABLE V. Common mode and differential mode frequency response performance under different PV access positions

	PV access busbar 1			PV access busbar 7		
Indicators	Scheme 1	Scheme 2	Scheme 3	Scheme 1	Scheme 2	Scheme 3
Maximum of $(f_2 - f_1)$ /Hz	0.046	0.035	0.046	0.047	0.035	0.046
Maximum of $(f_2 - f_3)$ /Hz	0.028	0.035	0.027	0.027	0.019	0.027
Maximum of $(f_1 - f_3)$ /Hz	0.029	0.007	0.022	0.021	0.016	0.020
Maximum of $((f_1 + f_2 + f_3)/3)$ /Hz	0.325	0.028	0.363	0.324	0.027	0.363
RoCoF	0.808	0.548	0.808	0.807	0.613	0.807

primary frequency modulation with inertia support scheme achieves the same steady-state frequency modulation effect while effectively improving frequency dynamic response, outperforming the VPPT frequency modulation scheme in technical performance. Specifically, the proposed control scheme not only reduces the rate of frequency change and the maximum frequency deviation but also suppresses the differential-mode component of frequency.

Small-signal model analysis of PV units participating in frequency regulation indicates that, compared with the VPPT frequency regulation scheme, the proposed control strategy improves the response of common-mode and differential-mode frequency components. Switching between VPPT and MPPT modes ensures that PV units will not operate in the left unstable region of the P-U curve following a sudden decrease in solar irradiance, thereby preventing negative impacts on frequency regulation.

ACKNOWLEDGMENT

This work was supported by Technology Project of State Grid Jiangsu Electric Power Co., Ltd., J2024JC-06.

REFERENCES

[1] Y. Wen, W. Yang, R. Wang, *et al.*, "Review and prospect of toward 100% renewable energy power systems," *Proceeding of the CSEE*, vol. 40, no. 6, pp. 1843–1855, 2020.

[2] W. Ma, "Thoughts on the development of frontier technology in electrical engineering," *Transactions of China Electrotechnical Society*, vol. 36, no. 22, pp. 4627–4636, 2021.

[3] Y. Fang, "Reflections on Frequency Stability Control Technology Based on the Blackout Event of 9 August 2019 in UK," *Automation of Electric Power Systems*, vol. 43, no. 24, pp. 1–5, 2019.

[4] C. Zhong, S. Zhou, G. Yan, *et al.*, "A new frequency regulation control strategy for photovoltaic power plant based on variable power reserve level control," *Transaction of China Electrotechnical Society*, vol. 34, no. 5, pp. 1013–1024, 2019.

[5] *GB/T 40595-2021*, Oct. 2021.

[6] L. Guo, M. Lei, Z. Yang, *et al.*, "Multi-objective coordinated control strategy for photovoltaic and energy-storage microgrid system," *Transaction of China Electrotechnical Society*, vol. 36, no. 19, pp. 4121–4131, 2021.

[7] Y. Li, T. Yao, X. Qiao, *et al.*, "Optimal configuration of distributed photovoltaic and energy storage system based on joint sequential scenario and source-network-load coordination," *Transaction of China Electrotechnical Society*, pp. 1–17, Jan. 14, 2022. DOI: 10.19595/j.cnki.1000-6753.tces.210712.

[8] C. Wen, Y. Huang, C. Hu, *et al.*, "Adaptive control of virtual impedance in parallel operation of virtual synchronous generator interface converter," *Transaction of China Electrotechnical Society*, vol. 35, no. S2, pp. 494–502, 2020.

[9] J. Li, J. Chen, W. Zhang, *et al.*, "Integrated control strategy for battery energy storage systems in distribution networks with high photovoltaic penetration," *Transaction of China Electrotechnical Society*, vol. 34, no. 2, pp. 437–446, 2019.

[10] Y. Gong, N. Li, and X. Liu, "Configuration method for capacity of energy storage in PV station considering wind power curtailment," *North China Electric Power*, no. 10, pp. 33–37, 2017.

[11] G. Liu, S. Lin, M. Wu, *et al.*, "Summary of virtual synchronous machine technology demonstration project," *Distribution & Utilization*, vol. 36, no. 4, pp. 37–42, 2019.

[12] H. D. Tafti, G. Konstantinou, C. D. Townsend, *et al.*, "Extended functionalities of photovoltaic systems with flexible power point tracking: recent advances," *IEEE Transactions on Power Electronics*, vol. 35, no. 9, pp. 9342–9356, 2020.

[13] H. D. Tafti, A. Sangwongwanich, Y. Yang, *et al.*, "An adaptive control scheme for flexible power point tracking in photovoltaic systems," *IEEE Transactions on Power Electronics*, vol. 34, no. 6, pp. 5451–5463, 2019.

[14] A. Sangwongwanich, Y. Yang, and D. Sera, "Delta power control strategy for multistring grid-connected PV inverters," *IEEE Transactions on Industry Applications*, vol. 53, no. 4, pp. 3862–3870, 2017.

[15] H. Zhang, X. Zhang, M. Li, *et al.*, "A photovoltaic virtual synchronous generator control strategy based on active power reserve," *Power System Technology*, vol. 43, no. 2, pp. 514–520, 2019.

[16] X. Yan, J. Lü, J. Jia, *et al.*, "Two-stage active standby photovoltaic virtual synchronous machine control strategy," *Power System Protection and Control*, vol. 48, no. 15, pp. 61–68, 2020.

[17] S. Wang, G. Sun, C. Yu, *et al.*, "Photovoltaic power generation system level rapid power control technology and its application," *Proceedings of the CSEE*, vol. 38, no. 21, pp. 6254–6263, 2018.

[18] J. Jia, X. Yan, Y. Wang, *et al.*, "Parameter identification and modelling of photovoltaic power generation systems based on LVRT tests," *IET Generation, Transmission & Distribution*, vol. 14, no. 15, pp. 3089–3098, 2020.

[19] W. A. Omran, M. Kazerani, and M. M. A. Salama, "Investigation of methods for reduction of power fluctuations generated from large grid-connected photovoltaic systems," *IEEE Transactions on Energy Conversion*, vol. 26, no. 1, pp. 318–327, 2011.

[20] X. Yan, Z. Song, S. Cui, *et al.*, "Primary frequency regulation strategy of doubly-fed wind turbine based on variable power point tracking and supercapacitor energy storage," *Transactions of China Electrotechnical Society*, vol. 35, no. 3, pp. 530–541, 2020.

[21] T. Zhao, Z. Lü, G. Liu, *et al.*, "Interpretation of virtual synchronous machine technology series standards," *Distribution & Utilization*, vol. 36, no. 4, pp. 13–17, 36, 2019.

[22] Z. Ma, X. Li, Z. Tan, *et al.*, "Integrated Control of primary frequency regulation considering dead band of energy storage," *Transactions of China Electrotechnical Society*, vol. 34, no. 10, pp. 2102–2115, 2019.

[23] H. Yuan, X. Yuan, and J. Hu, "Modeling of Grid-connected VSCs for power system small-signal stability analysis in DC-link voltage control timescale," *IEEE Transactions on Power Systems*, vol. 32, no. 5, pp. 3981–3991, 2017.

[24] J. Fang, R. Zhang, and H. Li, "Frequency derivative-based inertia enhancement by grid-connected power converters with a frequency-locked-loop," *IEEE Trans. Smart Grid*, vol. 10, no. 5, pp. 4918–4927, 2019.

[25] H. Gao, H. Xin, L. Huang, *et al.*, "Characteristic Analysis and Quantification of Common Mode Frequency in Power Systems With High Penetration of Renewable Resources," *Proceedings of the CSEE*, vol. 41, no. 3, pp. 890–900, 2021.

[26] L. Pagnier and P. Jacquod, "Optimal placement of inertia and primary control: A matrix perturbation theory approach," *IEEE Access*, vol. 7, pp. 145889–145900, 2019.

[27] J. Jia, X. Yan, P. Yang, *et al.*, "Circuit Modeling Method of Active Power-frequency Dynamics for Multiple-VSC Systems," *Proceedings of the CSEE*, vol. 42, no. 5, pp. 1933–1945, 2022.

[28] S. Dong and Y. C. Chen, "A Method to Directly Compute Synchronverter Parameters for Desired Dynamic Response," *IEEE Tran. Energy. Convers.*, vol. 33, no. 2, pp. 814–825, 2018.

[29] X. Yan, B. Liang, J. Jia, *et al.*, "Strategies to Increase the Transient Active Power of Photovoltaic Units during Low Voltage Ride Through," *Energies*, vol. 14, no. 17, p. 5236, 2021.

[30] X. Yan, C. Wang, A. Rasool, *et al.*, "Power reserve control strategy in the left-side of maximum power point for primary frequency regulation of grid-connected photovoltaic systems," *IET Power Electronics*, vol. 15, no. 2, pp. 93–108, 2022.

APPENDIX

TABLE A. Simulation parameters

Photovoltaic unit parameters		
Circuit parameters	Rated capacity P_N /MW	0.5
	Rated DC voltage /V	480
	Rated AC voltage /V	250
	Filter inductor L_f /mH	0.06
	Filter capacitor C_f /mF	5.1
Control parameters	Primary frequency regulation coefficient $k_f/(\mathrm{Hz}\cdot\mathrm{W}^{-1})$	2.5×10^5
	Inertia coefficient $k_H/(\mathrm{W}\cdot\mathrm{s}\cdot\mathrm{Hz}^{-1})$	3.1×10^5
	Filter time constant τ_f /s	0.01
	Time delay constant τ_0 /s	0.5
	Derating ratio d /%	10
Synchronous generator parameters		
	Capacity SG1, SG2 /MW	1
	Inertia coefficient K_{J1}, K_{J2} /(kg·m^2)	28.1, 70.3
	Damping coefficient K_{D1}, K_{D2} /(N·m·s·rad^{-1})	0
	Droop coefficient $R_{\omega1}, R_{\omega2}$ /pu	0.025